# Single-Input Broadband Hybrid Doherty Power Amplifiers Design Relying on a Phase Sliding-Mode of the Load Modulation Scheme

Chenyu Liang<sup>®</sup>, *Member, IEEE*, Patrick Roblin<sup>®</sup>, *Senior Member, IEEE*, Yunsik Hahn<sup>®</sup>, *Graduate Student Member, IEEE*, Jose I. Martinez-Lopez<sup>®</sup>, *Member, IEEE*, Hsiu-Chen Chang<sup>®</sup>, *Graduate Student Member, IEEE*, and Vanessa Chen<sup>®</sup>, *Member, IEEE* 

Abstract—This work introduces a novel design theory for a single-input hybrid Doherty power amplifier (PA) inspired by the design space existing within the previously reported dual-input Doherty-Chireix (outphasing) continuum. Unlike the conventional  $\lambda/4$  Doherty PA inverter which only performs the correct load modulation at its center frequency, the hybrid Doherty PA (HDω-PA) combiner network achieves a wideband load modulation using the frequency dependence of the electrical length of the output combiner lines versus frequency for sliding the PA mode of operation. A modified theory is presented in this work to allow for a single-input PA implementation. In this new design, the outphasing angle is only changing with frequency and not the input power. A transmission line phase shifter is used to provide the correct frequency-dependent input phase offset ensuring the correct wideband load modulation performed by the output combiner. A novel methodology is also proposed to select the optimal input phase offset to reduce the variation in the saturation power versus frequency and minimize the circuit size. A proof-of-concept demonstrator PA circuit is designed to operate from 2.5 to 3.3 GHz. When the fabricated PA is excited by a 20-MHz long-term evolution (LTE) modulated signal with 6-dB peak-to-average-power ratio (PAPR), an average efficiency of 45%-59% and adjacent channel leakage ratio (ACLR) less than -50 dBc are achieved after digital predistortion (DPD)

Manuscript received 2 August 2022; revised 4 October 2022; accepted 21 October 2022. This work was supported in part by the NSF under Grant 1952907 and in part by the Programa de Apoyos para la Superación del Personal Académico de la UNAM (DGAPA-PAPIIT) under Grant IN111522. This paper is an expanded version from the 22nd Annual IEEE Wireless and Microwave Technology Conference, held at Clearwater Beach, Florida on April 27–28, 2022. (Corresponding author: Patrick Roblin.)

Chenyu Liang was with the Department of Electrical and Computer Engineering, The Ohio State University, Columbus, OH 43210 USA. He is now with Qorvo US Inc., San Jose, CA 95134 USA.

Patrick Roblin and Yunsik Hahn are with the Department of Electrical and Computer Engineering, The Ohio State University, Columbus, OH 43210 USA (e-mail: roblin.1@osu.edu).

Jose I. Martinez-Lopez is with the Division de Ingenieria Electrica, Universidad Nacional Autonoma de Mexico, Mexico City 04510, Mexico.

Hsiu-Chen Chang was with the Department of Electrical and Computer Engineering, The Ohio State University, Columbus, OH 43210 USA. He is now with Skyworks Solutions, Irvine, CA 92617 USA.

Vanessa Chen is with the Department of Electrical and Computer Engineering, Carnegie Mellon University, Pittsburgh, PA 15213 USA.

Color versions of one or more figures in this article are available at https://doi.org/10.1109/TMTT.2022.3222355.

Digital Object Identifier 10.1109/TMTT.2022.3222355

across the entire band. When the fabricated PA is excited by a 5G-like 50-MHz orthogonal frequency-division multiplexing (OFDM) signal with 10-dB PAPR, an average efficiency of 33%-41% and ACLR less than -44 dBc are achieved after DPD across the entire band.

Index Terms—Doherty power amplifiers (PAs), Doherty-outphasing continuum, wideband PAs.

#### I. INTRODUCTION

**D**OHERTY power amplifiers (PAs) continue to draw attention from PA designers due to their enhanced back-off power efficiency and simple circuit topology. They have been widely adopted in wireless transmitter systems and are still a popular choice for the fifth-generation (5G) or beyond of wireless base station infrastructures. The conventional Doherty PA from [1] and [5] relies on the load modulation technique to maintain high efficiency from backoff to peak power level. The load modulation scheme depends on a quarter-wave  $(\lambda/4)$ transmission line (TL), which is inherently narrowband. In [6], a narrowband Doherty PA output combiner was developed based on a "black-box" type of a two-port network to facilitate the design process. Recently, there have been numerous efforts to extend the bandwidth of Doherty PAs [7], [8], [10], [11], [13], [14], [15], [16], [17], [18], [19], [20], [21], [22], [23], [23], [24], [44]. For example, in [14] a post harmonic matching network is designed to create the harmonic load modulation between main and auxiliary PAs, resulting in a broadband Doherty PA operation. In [19], an additional TL is incorporated at the auxiliary PA branch to obtain the desired AM-PM performance within a large bandwidth. Two extra TLs are inserted in the main and auxiliary PA branches in [22] to keep the backoff impedance seen by the main PA constant across the frequency band. From [25] to [34], there have also been many other advanced load modulation techniques proposed to break through PA bandwidth limitation. In particular, the distributed efficient PA and the load-modulated balanced amplifier have been showing promising wideband performance.

In addition, dual-input PAs have been investigated in [35], [36], [37], [38], [39], [40], and [41] for bandwidth extension.

0018-9480 © 2022 IEEE. Personal use is permitted, but republication/redistribution requires IEEE permission. See https://www.ieee.org/publications/rights/index.html for more information.

In [36], a Doherty-outphasing PA continuum was first proposed to design wideband PA output combiners with variable electrical lengths and characteristic impedance. Multidimensional computer-aided numerical search was then performed to select the desired PA output combiner structure which yields the largest bandwidth. From our recent research, the analytic Doherty-Chireix/outphasing continuum theory is introduced in [38]. Instead of relying on the computer simulations, closed-form design equations defining the Doherty-Chireix/outphasing continuum are carried out in this work. Two narrowband dual-input PAs combining both the features of Doherty and mixed-mode outphasing load modulation were designed in [38] and [46], both of which yield high efficiency over a large output power back-off (OBO) range. Furthermore, an analytic dual-input PA prototype is proposed as shown in [38, Fig. 3], which provides a systematic approach for the wideband dual-input PA design at the current-source reference planes. Thereafter, the work reported in [40] presents a wideband dual-input hybrid Doherty-outphasing PA solution by continuously varying, as the frequency changes, the load modulation mode measured by the auxiliary peak-to-backoff voltage ratio within the Doherty-Chireix continuum [38] while turning off the auxiliary transistor at backoff. Note that as the frequency increases, the mode of operation is targeted to vary from the HDmax outphasing mode [38] to the Doherty mode. The HDmax mode is an outphasing mode for which the main and auxiliary PAs provide the same peak power with OBO larger than 6 dB. The HDmax mode also exhibits high power efficiency between peak and backoff owing to its auxiliary peak-to-backoff voltage ratio, which remains constant to be unity versus output power. Compared with HDmax PA, the Doherty PA with the same OBO exhibits a noted slump in efficiency between peak and backoff

In [41], a comprehensive review of the analytic Doherty– Chireix/outphasing continuum theory and the PA demonstrator circuits designed to validate the theory was presented. This article also summarized the important closed-form equations used to design dual-input PA narrow/wideband output combiners from [38], [39], [40], [41]. However, compared with the dual-input PA architecture which requires careful and time-consuming input source synchronization and calibration, the single-input PA structure is simpler to design, operate, and thus more attractive, especially in industry, due to its lower cost. The main novelty of this work compared with the work reviewed in [41] is to address the complexity issue in the conversion of the dual-input operation into a single-input PA operation while still relying on the Doherty-Chireix/outphasing continuum concept summarized in [41] for expanding the bandwidth. Several solutions for the output combiner design are possible such as the constant OBO and the constant saturated power by selecting different frequency dependence for  $K_{va}$  and the electrical lengths. Furthermore, instead of determining the key frequency design parameter  $K_{va}(\omega)$  by trial and error as we did in [40], analytic formulas for both the cases of the constant OBO and the constant saturated power designs are derived in this work for the first time to synthesize the targeted linear and quasi-linear

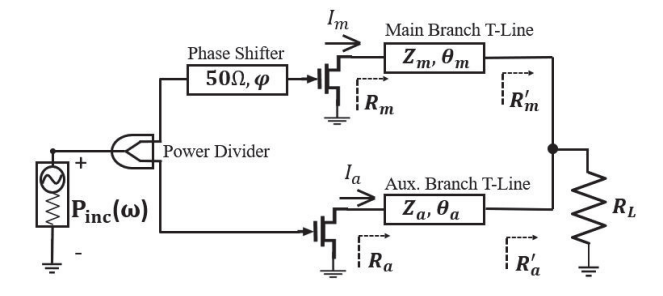


Fig. 1. Conceptual diagrams of the proposed single-input hybrid Doherty PA.

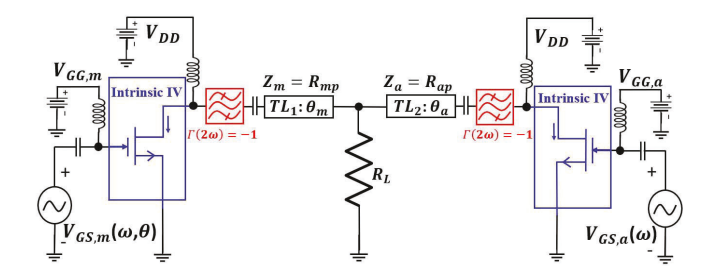


Fig. 2. Simulation schematic of the dual-input PA built with the nonlinear embedding device intrinsic IV model [45] and TL-based output combiner.

frequency dispersion for the electrical lengths  $\theta_m$  and  $\theta_a$  of the main and auxiliary branches, respectively.

The organization of this work is as follows. A single-input broadband hybrid Doherty PA ( $HD\omega$ -PA) combiner theory including the PA output combiner and input phase shifter design is presented in Section II. The design of a wideband  $HD\omega$ -PA demonstrator circuit is presented in Section III, and the simulation and measurement results are presented in Section IV. The achievements are summarized in Section V.

# II. WIDEBAND SINGLE-INPUT HYBRID DOHERTY CONTINUUM PA DESIGN THEORY

The conceptual diagram for the proposed single-input  $HD\omega$ -PA is shown in Fig. 1. Note that this prototype  $HD\omega$ -PA circuit presents the targeted operation at the current-source reference planes (CSRPs) for both the main and auxiliary transistor IV characteristics represented by the fieldeffect-transistor symbols as shown in Fig. 2. The proposed  $HD\omega$ -PA output combiner prototype consists of two TLs with the characteristic impedance of  $Z_m$  and  $Z_a$  and electrical length of  $\theta_m(\omega)$  and  $\theta_a(\omega)$ , respectively. The common load  $R_L$ connected in between the lines assists with the load modulation while delivering the output power. The main and auxiliary transistors are operating in class AB (or class B) and C modes with the second-harmonic current shorted, respectively. The gate of the transistors is driven by two voltage sources, with the one on the main side phase shifted by the outphasing angles  $\theta$  relatively. For the single-input HD $\omega$ -PA discussed in this work, a 50- $\Omega$  TL with electrical length  $\theta(\omega)$  is inserted to function as a frequency-dependent phase shifter.

# A. Design of the Phase Sliding-Mode Output Combiner

An important design parameter introduced in the Doherty-Chireix/Outphasing continuum solutions [38], [40] is the

peak-to-backoff drain voltage ratio of the auxiliary PA. It is defined as  $K_{va} = |V_{ap}|/|V_{ab}|$ , where the subscript a refers to the auxiliary PA, and the subscripts p and b refer to the peak and backoff power levels, respectively. For the theoretical analysis in this work, the auxiliary PA is fully turned off below backoff power, and thus, the peak-to-average drain current ratio of the auxiliary PA is very large and taken as infinity:  $K_{ia} = |I_{ap}|/|I_{ab}| = \infty$ . Based on (10) and (14) in [38], the asymmetry power ratio between the main and auxiliary PAs n simplifies to

$$n(\omega) = K_{va}(\omega) \frac{\text{OBO} - 1}{\text{OBO} + K_{va}(\omega)}$$
 (1)

where OBO is defined as the output backoff power range. It is worth mentioning that different from the PA designed in [40], where the OBO is set to be varying from 6 to 9.54 dB versus frequency, the OBO in this work is set to remain constant at 8 dB versus frequency. This requires a slight variation in the output load  $R_L$  and peak auxiliary load  $R_{ap}$  versus frequency. The line electrical lengths  $\theta_m$  and  $\theta_a$ , and the input phase offset  $\theta$  will be expressed in terms  $K_{va}$  to accommodate the single-input Doherty PA design. The characteristic impedances for the TLs— $Z_m$ ,  $Z_a$ , and the output load  $R_L$ —remain themselves as in [38] to maintain a broadband operation at peak power

$$Z_{m} = R_{mp}$$

$$Z_{a}(\omega) = R_{ap}(\omega)$$

$$R_{L}(\omega) = \frac{R_{mp}}{n(\omega) + 1} = \frac{R_{mp}(OBO/K_{va}(\omega) + 1)}{OBO - 1}$$
(2)

where  $R_{mp}$  and  $R_{ap}(\omega)$  refer to the loads at CSRP to be provided at peak power seen by the main and auxiliary devices, respectively.

The dual-input PA outphasing angles at backoff  $\theta_b$  and peak power level  $\theta_p$  which are given by (17) and (18) in [38] are expressed in terms of only  $K_{va}$  and OBO with  $K_{ia} = \infty$ , yielding

$$\theta_b(\omega) = \pm \cos^{-1} \left( \pm \sqrt{\frac{\text{OBO} - K_{va}^2(\omega)}{\text{OBO} + 2K_{va}(\omega) + 1}} \right)$$

$$\theta_p(\omega) = \pi - \theta_b(\omega). \tag{3}$$

For each value of  $K_{va}$ , there exists four possible combinations (eight solutions) for the input phase offset angles based on (3)

$$\theta_{b1} = \cos^{-1}\left(\sqrt{\frac{OBO - K_{va}^{2}(\omega)}{OBO + 2K_{va}(\omega) + 1}}\right); \theta_{p1} = \pi - \theta_{b1}$$

$$\theta_{b2} = \cos^{-1}\left(-\sqrt{\frac{OBO - K_{va}^{2}(\omega)}{OBO + 2K_{va}(\omega) + 1}}\right); \theta_{p2} = \pi - \theta_{b2}$$

$$\theta_{b3} = -\cos^{-1}\left(\sqrt{\frac{OBO - K_{va}^{2}(\omega)}{OBO + 2K_{va}(\omega) + 1}}\right); \theta_{p3} = \pi - \theta_{b3}$$

$$\theta_{b4} = -\cos^{-1}\left(-\sqrt{\frac{OBO - K_{va}^{2}(\omega)}{OBO + 2K_{va}(\omega) + 1}}\right); \theta_{p4} = \pi - \theta_{b4}.$$

The electrical lengths  $\theta_m$  and  $\theta_a$  in Fig. 1 are simplified and expressed in terms of  $K_{va}$  and OBO as

$$\theta_m(\omega) = \tan^{-1} \left( \frac{K_{va}(\omega) + \text{OBO}}{K_{va}(\omega) + 1} \tan \theta_b(\omega) \right)$$
 (4)

$$\theta_a(\omega) = \tan^{-1} \left( \frac{K_{va}(\omega) - \text{OBO}/K_{va}(\omega)}{K_{va}(\omega) + 1} \tan \theta_b(\omega) \right). \quad (5)$$

Having established the relationships between the electrical lengths  $\theta_m(\omega)$  and  $\theta_a(\omega)$ , the targeted OBO and  $K_{va}(\omega)$  from (4) and (5). The frequency dependence for  $K_{va}(\omega)$  can be theoretically obtained to yield frequency-dependent solution for the TL electrical lengths  $\theta_m(\omega)$  and  $\theta_a(\omega)$ .

First, by selecting the desired extreme  $K_{va}(\omega_{\min})$  and  $K_{va}(\omega_{\max})$ , (3) and (4) can be used to determine the boundary conditions  $\theta_m(\omega_{\min})$  and  $\theta_m(\omega_{\max})$  for the targeted OBO. One can then assume a linear dispersion for the main TL electrical length  $\theta_m(\omega)$  as  $\omega$  varies from  $\omega_{\min}$  to  $\omega_{\max}$ 

$$\theta_m(\omega) = (1 - \alpha)\theta_m(\omega_{\min}) + \alpha\theta_m(\omega_{\max}) \tag{6}$$

where  $\alpha = (\omega - \omega_{\min})/(\omega_{\max} - \omega_{\min})$  varies from 0 to 1 with frequency. Equation (3) can then be reformulated to:  $\tan^2 \theta_b = (K_{va} + 1)^2/(-K_{va}^2 + \text{OBO})$ . Starting from (4), a quadratic equation for  $K_{va}$  is formed in terms of OBO and  $\theta_m(\omega)$ , which is given by

$$(\tan^2 \theta_m + 1) K_{pq}^2 + 2 \text{OBO} K_{pq} + \text{OBO}(\text{OBO} - \tan \theta_m^2) = 0.$$

This quadratic equation admits for solution

$$K_{va}(\theta_m, OBO) = \frac{-b + \sqrt{b^2 - 4ac}}{2a} \text{ with}$$

$$a = \tan \theta_m^2 + 1$$

$$b = 2 \text{ OBO}$$

$$c = OBO(OBO - \tan \theta_m^2). \tag{7}$$

Taking the ratio of (5) by (4), the required dispersion  $\theta_a(\omega)$  for the auxiliary TL, which might be slightly nonlinear, is then given by

$$\tan \theta_a(\omega) = \tan \theta_m(\omega) \frac{K_{va}(\omega) - \text{OBO}/K_{va}(\omega)}{K_{va}(\omega) + \text{OBO}}.$$
 (8)

In this work, OBO is fixed to 8 dB and  $K_{va}(\omega)$  is calculated to be {1.50, 1.75, 1.97, 2.15, 2.30, 2.40, 2.47, 2.51} as the frequency linearly increases from 2.5 to 3.2 GHz based on (7) and (6). The resulting electrical lengths  $\theta_m(\omega)$  and  $\theta_a(\omega)$  from (6) and (8), shown as red dots and blue rectangles in Fig. 8(b), are found to be quasi-linear functions of frequency as desired to closely fit the phase dispersion of the transmission-line-based output matching networks.

The four different cases based on different sign selection of (3) are plotted in Fig. 3. The absolute values of  $\theta_b$  and  $\theta_p$  are shown in Fig. 3(a) and (b), respectively. Based on (4) and (5), the electrical length for the main branch TL:  $\theta_m$  and auxiliary branch TL:  $\theta_a$  are also shown in Fig. 3(c) and (d), respectively. The two positive signs ( $\theta_{m1}$  and  $\theta_{a1}$ ) or the two negative signs ( $\theta_{m4}$  and  $\theta_{a4}$ ) should be selected to reduce the physical length of the two TLs ( $\theta_m$  and  $\theta_a$ ). In summary, once the frequency dependence of  $K_{va}(\omega)$  has been selected, the

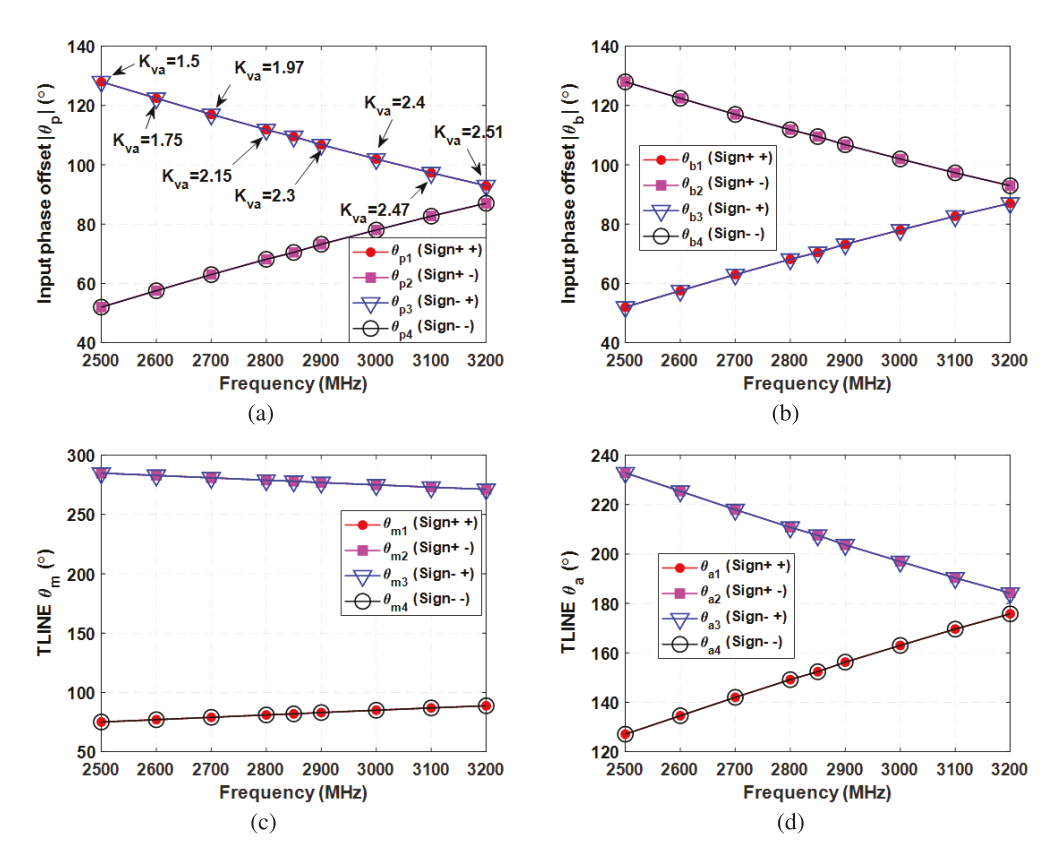


Fig. 3. (a) Theoretical outphasing angle  $|\theta_p|$  versus frequency, (b) theoretical outphasing angle  $|\theta_b|$  versus frequency, (c) theoretical electrical length  $\theta_m$  versus frequency, and (d) theoretical electrical length  $\theta_a$  versus frequency.

design of the  $HD\omega$ -PA output combiner prototype shown in Fig. 2 is complete.

It is worth mentioning that for the operation of the dualinput PAs, the outphasing angle  $\theta$  needs to be varied gradually from  $\theta_b$  to  $\theta_p$  as the output power increases from backoff to peak power. However, to implement a single-input PA, the outphasing angle has to remain power-independent if it is to be realized with a passive input phase shifter circuit. The design of the input phase shifter will be discussed in Section II-B. By sliding the value of  $K_{va}$ , one obtains a continuum of solutions for the HDω-PA output combiner, all maintaining the desired load modulation behavior from the Doherty PA mode to the HDmax PA mode introduced in [38]. However, to design a single-input  $HD\omega$ -PA capable of operating across a wide range of frequencies, one needs to synthesize the frequency dependence of  $K_{va}(\omega)$  such that the required  $HD\omega$ -PA output combiner is realizable while also maintaining a constant OBO. This is readily achieved if the combiner's TLs exhibit quasi-linear dispersion  $\theta_m(\omega)$  and  $\theta_a(\omega)$ , as will be discussed next in Section III.

## B. Input Phase Shifter Design

In this work, where the Doherty to HDmax continuum mode in [38] is selected, it further assumes that the auxiliary device is completely turned off below the backoff power level  $(K_{ia} = \infty)$ , while the value of  $K_{va}$  is sliding from the Doherty to HDmax PA modes. Hence, only the main device is actively

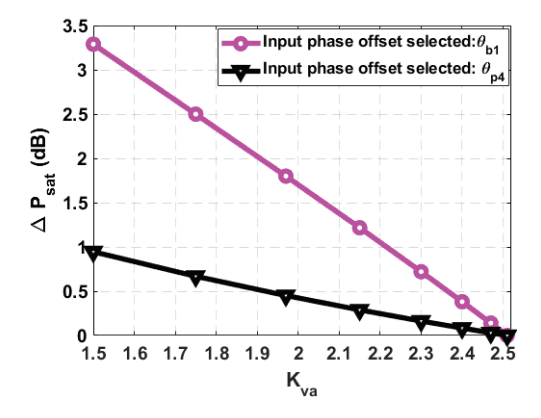


Fig. 4. Theoretical analysis on the saturation power variation by selecting different input outphasing angles:  $\theta_{p4}(\omega)$  and  $\theta_{b1}(\omega)$ .

operating below the backoff power. Thereby, the outphasing angle value at backoff has an insignificant impact on the PA's overall backoff efficiency since the main amplifier, which is typically biased at class-B/AB mode, is dominating the PA performance at backoff. It is then reasonable to keep the input outphasing angle  $\theta$  constant between peak and backoff to realize the desired single-input PA at each frequency. As the electrical length of the main and auxiliary TLs has been determined in the previous subsection, from Fig. 3(a) and (b) there are eight candidates for the outphasing angles remaining to be selected as the input phase offset:  $\theta_{bi}$  and  $\theta_{pi}$ . To reduce the physical length of the input phase shifter,  $\theta_{b1}$ ,

TABLE I SUMMARY OF THE DESIGN PARAMETERS FOR THE HD $\omega$ -PA PROTOTYPE

$f_0$	2.5 GHz	2.6 GHz	2.7 GHz	2.8 GHz	2.9 GHz	3.0 GHz	3.1 GHz	3.2 GHz
$K_{va}(\omega)$	1.50	1.75	1.97	2.15	2.30	2.40	2.47	2.51
$\theta(\omega)$	$52.0^{\circ}$	$57.5^{\circ}$	$63.0^{\circ}$	$68.2^{\circ}$	$73.2^{\circ}$	$78.0^{\circ}$	$82.7^{\circ}$	$87.0^{\circ}$
$R_{mp}$	24.4 $\Omega$	24.4 $\Omega$	24.4 $\Omega$	24.4 $\Omega$				
$R_{mb}(\omega)$	$76.3~\Omega$	71.6 $\Omega$	$68.1 \Omega$	$65.6 \Omega$	$63.8 \Omega$	$62.6 \Omega$	$61.8 \Omega$	$61.5 \Omega$
$R_{ap}(\omega)$	$23.9 \Omega$	$21.2 \Omega$	$19.3 \Omega$	$18.1 \Omega$	$17.3 \Omega$	$16.7 \Omega$	$16.4~\Omega$	$16.2 \Omega$
$\hat{Z}_m$	$24.4~\Omega$	24.4 $\Omega$	24.4 $\Omega$	24.4 $\Omega$	24.4 $\Omega$	24.4 $\Omega$	24.4 $\Omega$	24.4 $\Omega$
$Z_a(\omega)$	$23.9 \Omega$	$21.2 \Omega$	$19.3 \Omega$	$18.1 \Omega$	$17.3 \Omega$	$16.7 \Omega$	$16.4 \Omega$	$16.2 \Omega$
$R_L(\omega)$	$12.1 \Omega$	$11.4 \Omega$	$10.8 \Omega$	$10.4 \Omega$	$10.1 \Omega$	$9.9~\Omega$	$9.8 \Omega$	$9.7~\Omega$
$\theta_m(\omega)$	$75.1^{\circ}$	$77.0^{\circ}$	$79.0^{\circ}$	$80.5^{\circ}$	$83.0^{\circ}$	$85.3^{\circ}$	$87.3^{\circ}$	88.8°
$\theta_a(\omega)$	$127.1^{\circ}$	$134.6^{\circ}$	$142.8^{\circ}$	$149.2^{\circ}$	$156.3^{\circ}$	163°	$169.6^{\circ}$	$175.8^{\circ}$

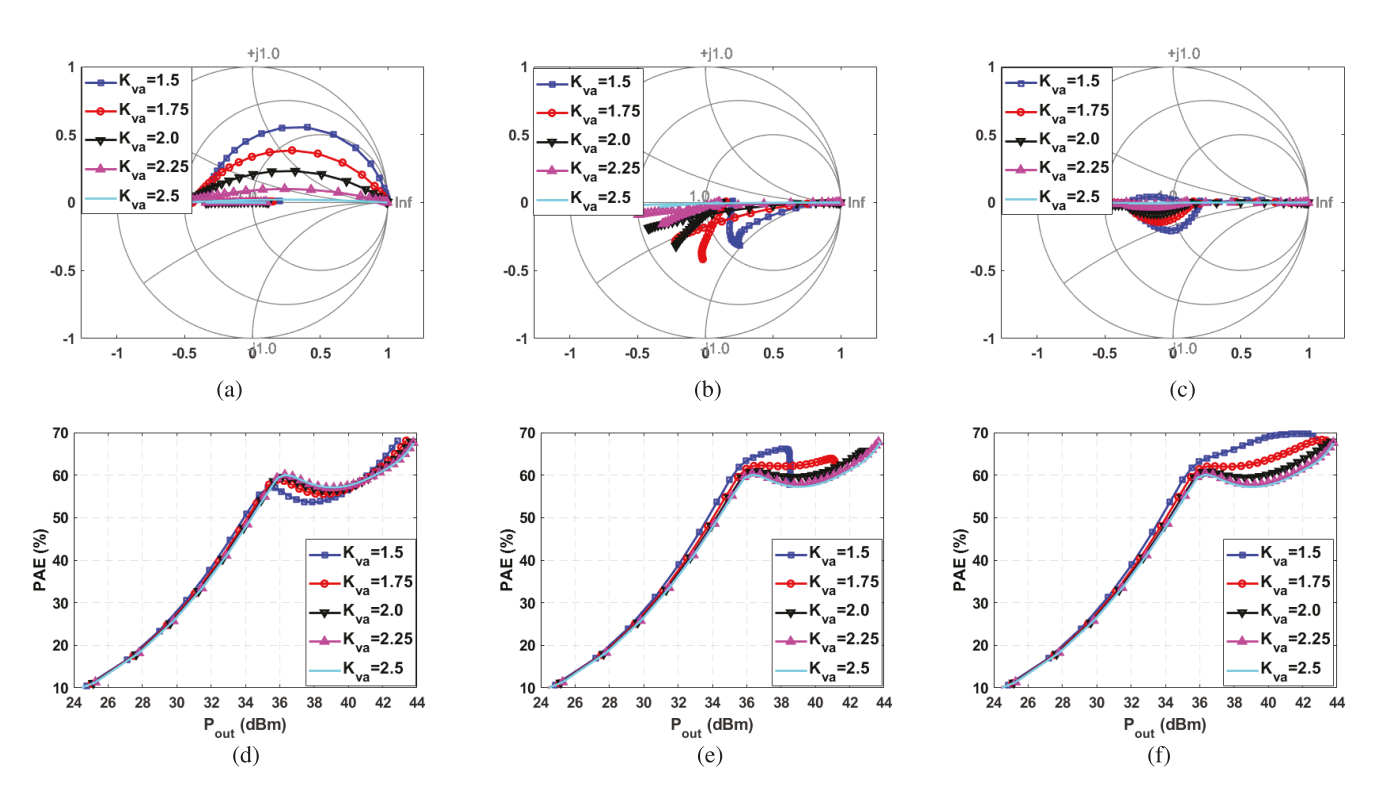


Fig. 5. Simulated load modulation trajectories and PAE versus  $K_{va}$  based on the ADS schematic depicted in Fig. 2. Case I: (a) load modulation and (d) PAE when  $\theta_{p4}$  is selected as the input phase offset. Case II: (b) load modulation and (e) PAE when  $\theta_{p1}$  is selected as the input phase offset. Case III: (c) load modulation and (f) PAE for when the outphasing angle varies from  $\theta_{b4}$  to  $\theta_{p4}$  with the output power [40]. (a) Case I: Load Modulation. (b) Case II: Load Modulation. (c) Case III: Load Modulation. (d) Case I: PAE. (e) Case III: PAE.

 $\theta_{b3}$ ,  $\theta_{p2}$ , or  $\theta_{p4}$  should be selected due to their smaller electrical length value. In Section II-A, we saw that either the solution  $\theta_{b1}$  or  $\theta_{p4}$  must be selected to reduce the physical length of the output combiner. Thus, to jointly reduce the physical length of both the phase shifter and the output combiner, the input phase offset  $\theta(\omega)$  must be selected to be either  $\theta_{b1}(\omega)$  or  $\theta_{p4}(\omega)$ .

It has been found that the choice of  $\theta_{b1}$  or  $\theta_{p4}$  also has an impact on the variation in the saturation power  $P_{\text{sat}}$  versus frequency. Plugging (1) from this work into (5) in [40], the Z-parameters of the HD $\omega$ -PA output combiner are simplified to be

$$\mathbf{Z} = \begin{bmatrix} R_{mb} & \frac{R_{ap}(\text{OBO}-1)}{K_{va}+1} e^{-j\theta_b} \\ \frac{R_{ap}(\text{OBO}-1)}{K_{va}+1} e^{-j\theta_b} & R_{ap}\beta \end{bmatrix}$$
(9)

with

$$\beta = \frac{1 + \frac{\text{OBO} + K_{\text{va}}}{K_{va}(K_{va} + 1)} + \frac{K_{va}^2 - \text{OBO}}{K_{va}(K_{va} + 1)} \cdot j \tan \theta_b}{1 + i \tan \theta_b}$$

The fundamental current defined as flowing out of the main PA is set as  $I_m = |I_m|$ , and the fundamental current defined as flowing out of the auxiliary PA is set as  $I_a = |I_a|e^{-j\theta}$ , where  $\theta$  refers to the input phase offset angle between the main and auxiliary PAs. It is noted that  $I_m$  and  $I_a$  are both power- and frequency-dependent; however,  $\theta$  is set to be only frequency-dependent. The fundamental voltages for the main PA  $V_m$  and for the auxiliary PA  $V_a$  are calculated by

$$V_m(K_{va}, \theta) = Z_{11} \cdot I_m + Z_{12} \cdot I_a$$
  
 $V_a(K_{va}, \theta) = Z_{12} \cdot I_m + Z_{22} \cdot I_a$ .

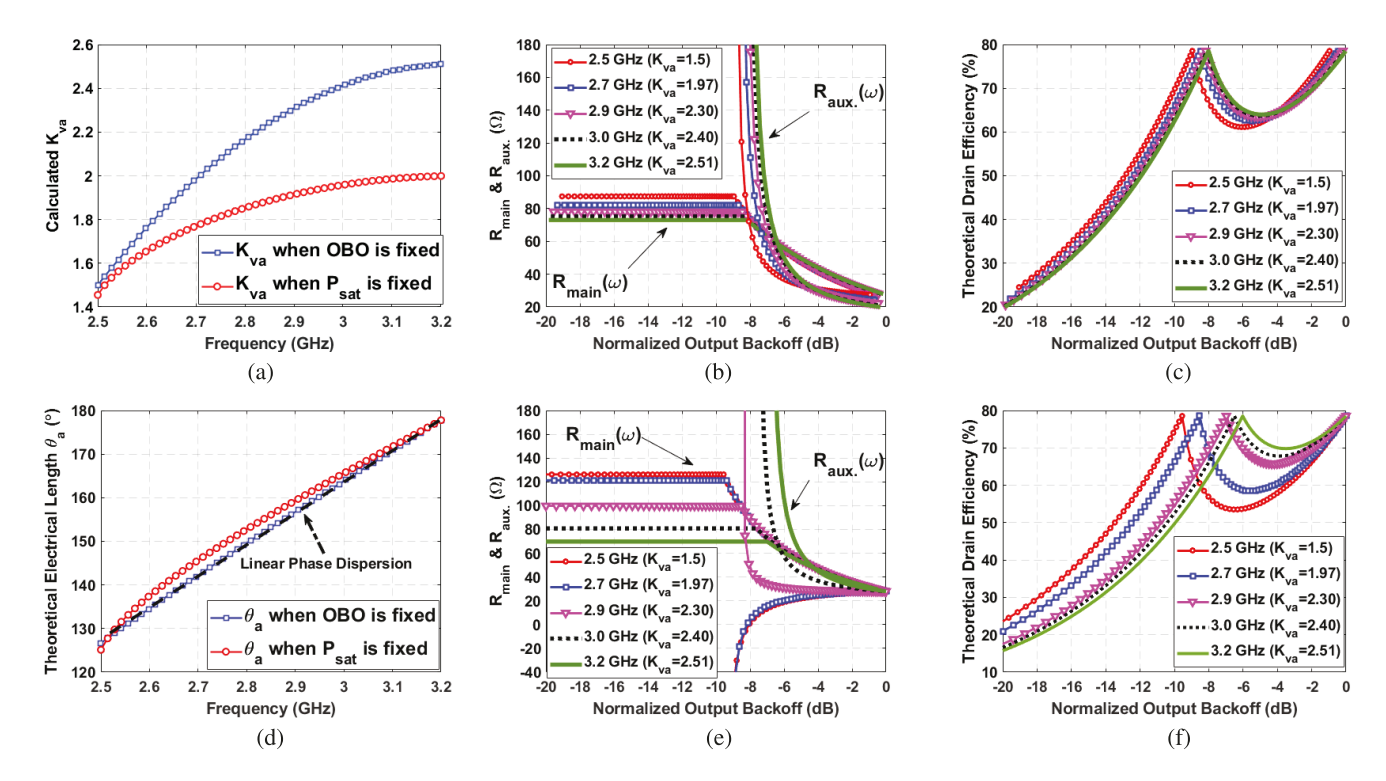


Fig. 6. Theoretical analysis comparing constant OBO and constant saturated power (constant n) designs in terms of (a) calculated  $K_{va}$  for both the cases, (b) calculated load for constant OBO, (c) calculated drain efficiency for constant OBO, (d) calculated  $\theta_a$  for both cases, (e) calculated load for constant saturated power, and (f) calculated drain efficiency for constant saturated power. (a)  $K_{va}$  Comparison. (b) Constant OBO. (c) Constant OBO. (d)  $\theta_a$  Comparison. (e) Constant  $P_{sat}$ .

The load-modulated impedance seen by the main and auxiliary devices and output power delivered by the  $HD\omega$ -PA output combiner are given by

$$Z_{mL}(K_{va}, \theta) = \frac{V_m}{I_m}; Z_{aL}(K_{va}, \theta) = \frac{V_a}{I_a}$$

$$P_{\text{out}}(K_{va}, \theta) = \frac{1}{2} \Re \{V_m I_m^*\} + \frac{1}{2} \Re \{V_a I_a^*\}.$$
 (10)

To observe the impact on the saturation power and load impedance caused by the input phase offset angle  $\theta$ , a theoretical analysis is performed to visualize the variation in  $P_{\text{out}}$ . The drain bias  $V_{DD}$  is set to be 25 V and  $I_{\text{max}}$  at 1.8 A across all the frequencies. Assuming the device knee voltage is  $V_k = 3 V$ , the fundamental voltage at peak power for the main and auxiliary PAs is  $|V_{mp}| = |V_{ap}| = V_{DD} - V_k = 22 \text{ V}$ . By sweeping  $K_{va}$  from 1.5 to 2.5, the variation in the saturation power  $\Delta P_{\text{sat}}$  is calculated, where  $\Delta P_{\text{sat}}$  is defined as

$$\Delta P_{\text{sat}} = |P_{\text{sat}}(K_{pa}) - \min(P_{\text{sat}}(K_{pa}))|. \tag{11}$$

As shown in Fig. 4, the magenta circles and black triangles indicate the variation in the saturation power  $\Delta P_{\rm sat}$  versus  $K_{va}$  when the input phase offset angle  $\theta_{b1}$  or  $\theta_{p4}$  is used, respectively. This clearly shows that  $\Delta P_{\rm sat}$  is smaller versus  $K_{va}$  (frequency) when  $\theta_{p4}$  is adopted.

To further demonstrate which outphasing angles— $\theta_{b1}$  or  $\theta_{p4}$ —should be selected as the constant input phase offset angle for optimal performance, three circuit harmonic balance simulations using advanced design system (ADS) are performed based on the circuits topology shown in Fig. 2. The resulting simulated load modulation trajectories and power-added efficiency (PAE) for the three cases are plotted

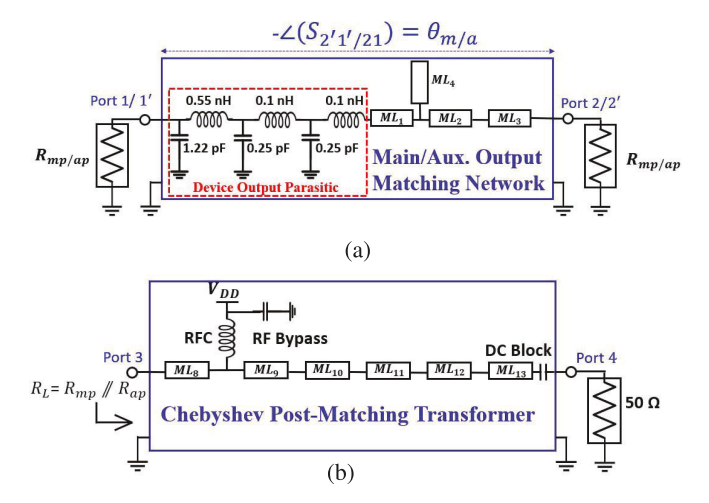


Fig. 7. (a) Synthesis of the effective overall electrical lengths of the main/auxiliary branches and the effective characteristic impedances of the main/auxiliary branches and (b) output postmatching transformer.

in Fig. 5. For case I, where the outphasing angle  $\theta$  is fixed at  $\theta_{p4}$  as the input power is increased, the saturation power level and the efficiency are similar to each other when sweeping  $K_{va}$  from 1.5 to 2.5. This agrees with the theoretical analysis performed in Fig. 4. However, for case II where the input phase is selected to be  $\theta_{b1}$ , the saturation power is around 4 dB less for  $K_{va} = 1.5$  compared with the saturation power for  $K_{va} = 2.5$ , as expected from the theoretical analysis as shown in Fig. 4. Intuitively, the saturation power loss is due to the improper load modulation behavior shown in Fig. 5(b) when

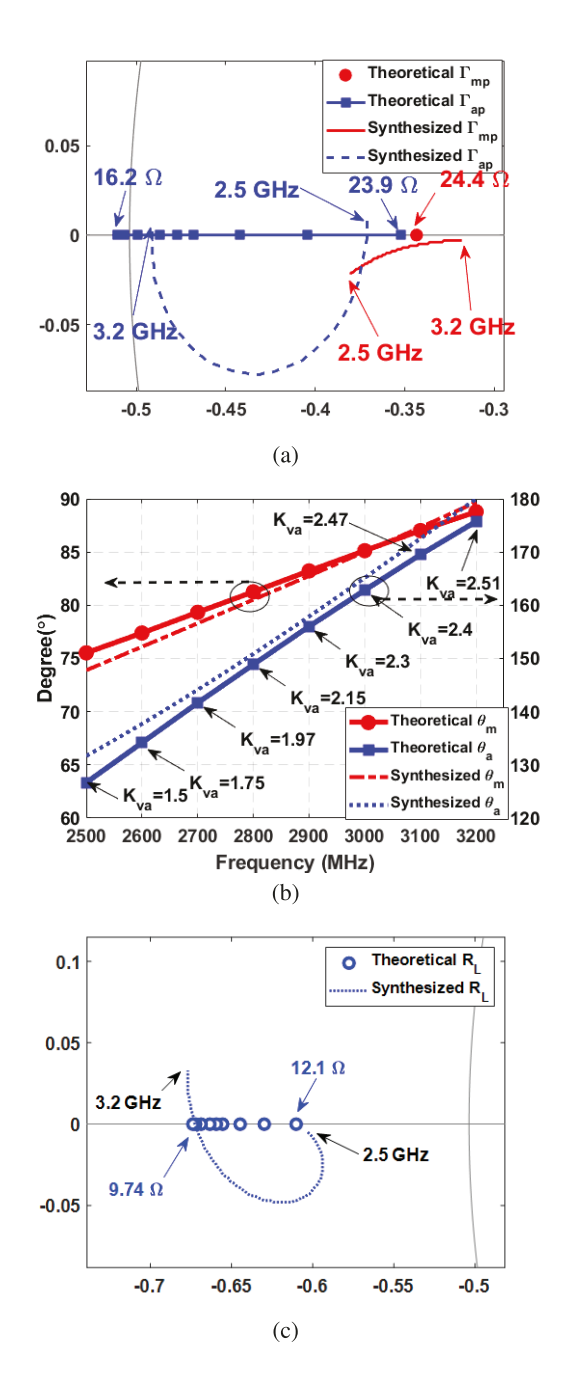


Fig. 8. (a) Synthesized load impedances seen by the main and auxiliary devices on the zoomed-in Smith chart, (b) synthesized electrical length of the output matching networks, and (c) synthesized  $R_L$  on the zoomed-in Smith chart.

the input phase offset  $\theta = \theta_{b4}$  deviates from  $\theta_a(\omega) - \theta_m(\omega)$ . Case III shown in Fig. 5(e) and (f) is used as a reference, where the outphasing angle is varied linearly from  $\theta_{b1}$  to  $\theta_{p4}$  as the incident power increases under each  $K_{va}$  value. Although there is a minor efficiency degradation in case I between the backoff and peak power regimes compared with the performance achieved by the reference dual-input PA prototype in case III, the backoff efficiencies and saturation powers obtained are similar in both the cases. Therefore, to design a wideband single-input PA with relatively constant saturation power, the input phase offset  $\theta(\omega)$  should be selected to be equal to  $\theta_{p4}(\omega)$  in (3). It is also worth mentioning that fine-tuning

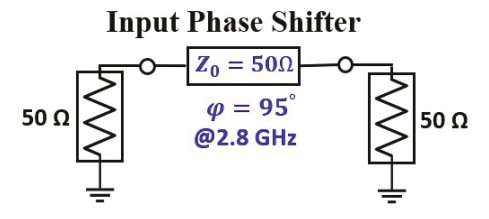


Fig. 9. TL-based input phase shifter.

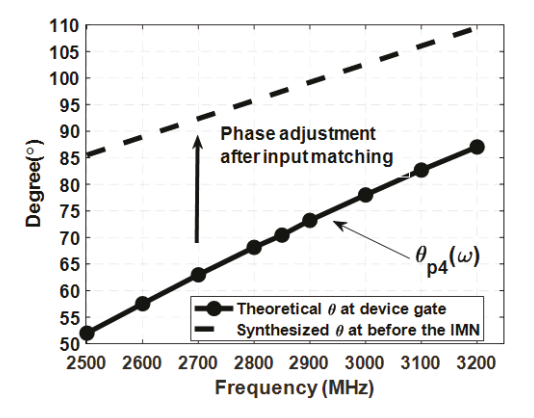


Fig. 10. Simulated input phase offset angles versus frequency.

around  $\theta_{p4}(\omega)$  could be performed to further minimize the saturation power variation versus frequency when the physical circuit is being implemented. Table I summarizes the targeted HD $\omega$ -PA design parameters predicted by the theory, which are used to guide the PA circuit design and optimization.

# C. Comparison of the PA Theoretical Performance

The case where OBO is fixed at 8 dB versus frequency has been extensively investigated in the above sections. However, it is also possible to convert the wideband dual-input PA reported in [40] for constant saturated power  $P_{\rm sat}$  into a single-input PA using different input phase shifter and output combiner designs. Indeed, the output combiner circuits in [40] were designed differently to keep an asymmetry power ratio n=1 constant for all the frequencies. By setting n=1 in (1), the saturation power remains constant as suggested by (15) in [38]. It results that OBO is given by: OBO =  $2K_{va}/(K_{va}-1)$ . A similar quadratic equation for  $K_{va}$  in terms of  $\theta_m(\omega)$  can also be formulated for the case of n=1

$$(1 + \tan^2 \theta_m) K_{va}^2 + (1 - 3 \tan^2 \theta_m) K_{va} + 2 \tan \theta_m^2 = 0.$$

Similar to (7),  $K_{va}$  can be calculated by taking the ratio of  $\tan \theta_m$  and  $\tan \theta_a$  given by (6) presented in [40], where the main TL electrical length  $\theta_m(\omega)$  is the user-defined linear dispersion given by (6). After solving the  $K_{va}$  quadratic equation, the auxiliary TL electrical length  $\tan \theta_a(\omega)$  is given by

$$\tan \theta_a(\omega) = \tan \theta_m(\omega) \frac{K_{va}(\omega) - 2}{K_{va}(\omega)}.$$
 (12)

The theoretical drain efficiency  $\eta$  versus the normalized backoff power can then be calculated for different  $K_{va}(\omega)$ .

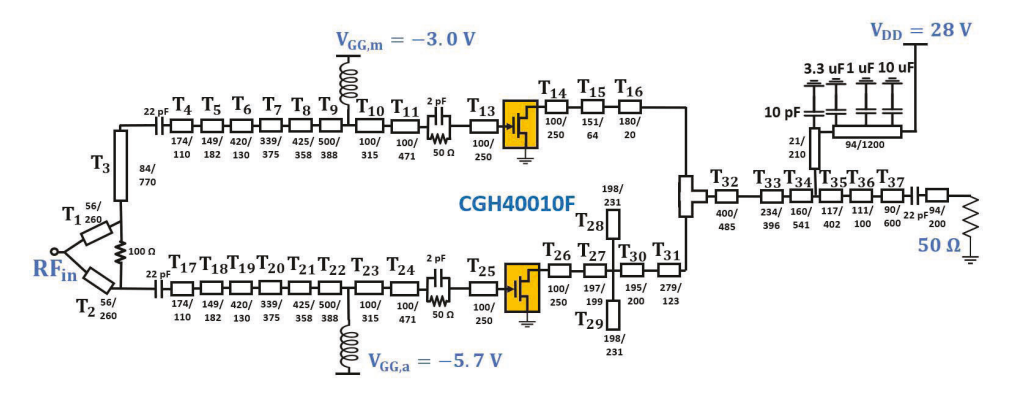


Fig. 11. Schematic of the proposed  $HD\omega$ -PA (unit: mils).

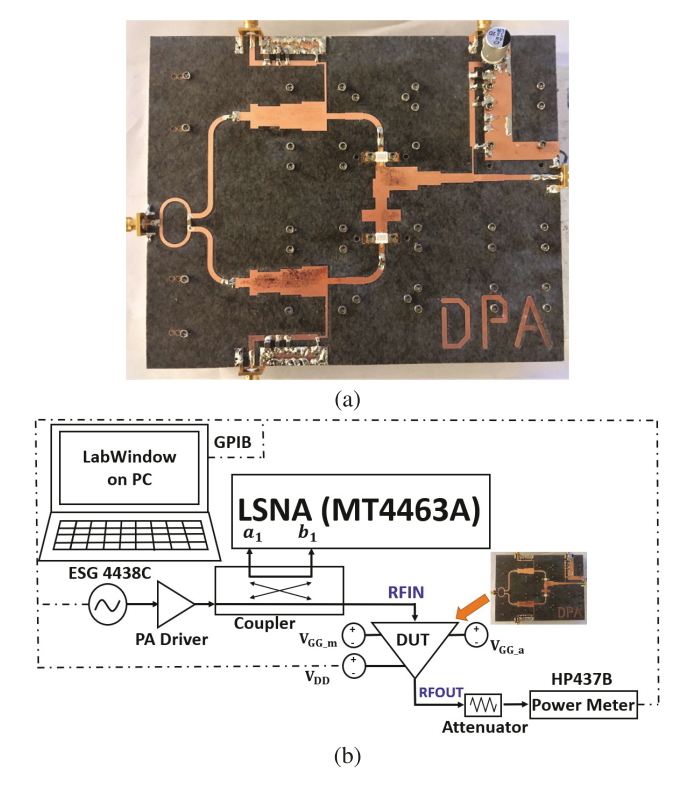


Fig. 12. (a) Fabricated wideband dual-input HD $\omega$ -PA demonstrator circuit and (b) LSNA test bench used for CW measurements.

By assuming ideal class-B operation for both the main and auxiliary PAs, the drain efficiencies  $\eta$  are given by:

$$\eta(K_{va}, P_{\text{out}}) = \frac{P_{\text{out}}}{P_{\text{dc}}} = \frac{\pi \left\{ \Re e \left\{ V_m I_m^* \right\} + \Re e \left\{ V_a I_a^* \right\} \right\}}{4 \ V_{DD} \left( |I_m| + |I_a| \right)}. \quad (13)$$

In this work, Case I is for OBO fixed at 8 dB for all the frequencies. To demonstrate several input designs are possible, we shall compare Case I with Case II where the asymmetry power ratio n is fixed at 1 (constant saturated power) for all the frequencies. To compare the theoretical performance between the two cases,  $K_{va}$  and theoretical electrical length  $\theta_a$  are plotted in Fig. 6(a) and (d), respectively. It is noted that the calculated frequency dispersion of  $\theta_a$  for Case I is less nonlinear than that for Case II, which makes it easier for implementing with the TL-based output matching circuits.

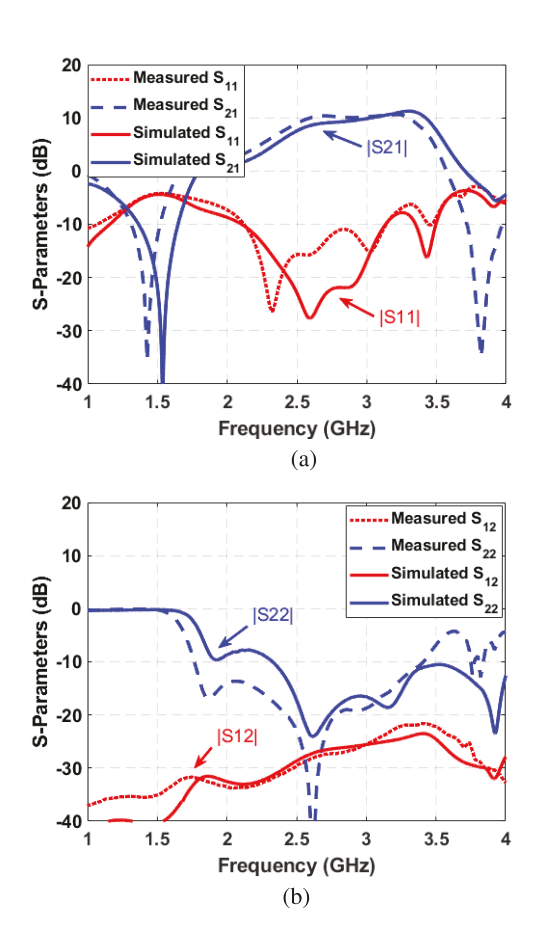


Fig. 13. Simulated versus measured small-signal performance. (a)  $|S_{11}|$  and  $|S_{21}|$ . (b)  $|S_{12}|$  and  $|S_{22}|$ .

The theoretical load-modulated impedances seen by the main and auxiliary devices for both the cases are shown in Fig. 6(b) and (e), respectively. The backoff impedance variation versus frequency of Case I is significantly smaller than that of Case II, which also facilitates the wideband impedance matching process in the final design realization. To better visualize the performance distinction between the two cases, the efficiency response versus power and frequency under both the cases are plotted in Fig. 6(c) and (f), respectively. Although Case II exhibits a constant saturation power in theory, the OBO varies by more than 3 dB as the frequency increases. Case I with fixed OBO design is adopted for a single-input wideband

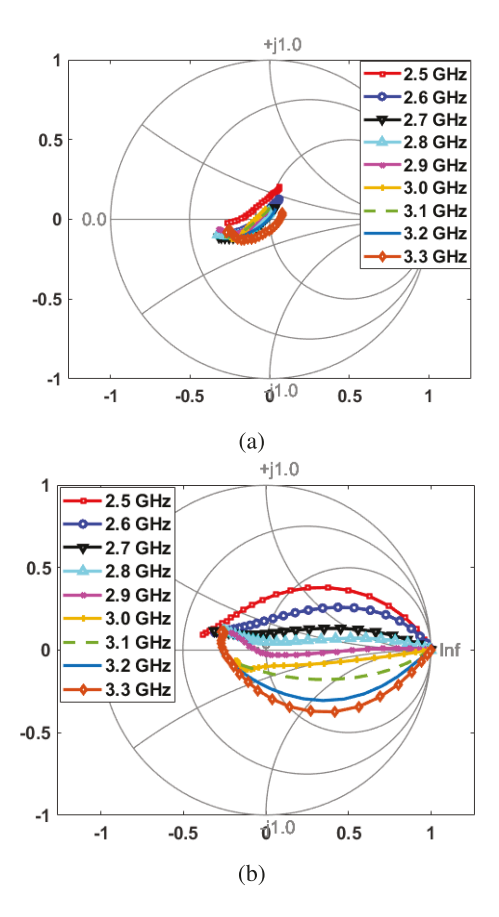


Fig. 14. (a) Simulated load trajectories versus frequency seen by the main PA and (b) simulated load trajectories versus frequency seen by the auxiliary PA. (a) Main PA. (b) Auxiliary PA.

PA design in this work, due to its more linear frequency dispersion of the electrical length and more closely grouped backoff impedances versus frequency.

# III. PA CIRCUITS DESIGN

To validate the proposed theory, a wideband HDω-PA demonstrator circuit operating from 2.5 to 3.2 GHz is designed and evaluated. The main and auxiliary PA branches are first designed and optimized using multisection TLs and open stub circuits as shown in Fig. 7(a). It is noted that the multisection TLs need to be optimized to simultaneously satisfy the targeted electrical dispersion and load impedance transformation from 2.5 to 3.2 GHz, while controlling the second-harmonic impedance to avoid the PAE minimum region. At peak power level, the impedances  $R_{mp}'$  and  $R_{ap}'$  seen at the combiner's junction point shown in Fig. 1 need to be transformed for all the frequencies to  $R_{mp}$  and  $R_{ap}$  seen by the main and auxiliary PAs, respectively. The target design goals for the impedance and electrical length versus frequency are summarized in Table I. It is noted in Table I that at peak power level, we have  $R'_{mp} = R_{mp}$  and  $R'_{ap} = R_{ap}$  across the entire band. The optimized main and auxiliary PA branches provide the impedance transformation from 2.5 to 3.2 GHz presented in the zoomed-in Smith chart Fig. 8(a). The red solid line refers to the simulated  $R_{ap}$  across the frequency and the red dot refers to the theoretical  $R_{ap}=24.4~\Omega$ . The blue dashed line refers to the simulated  $R_{mp}$  across the frequency, which are carefully

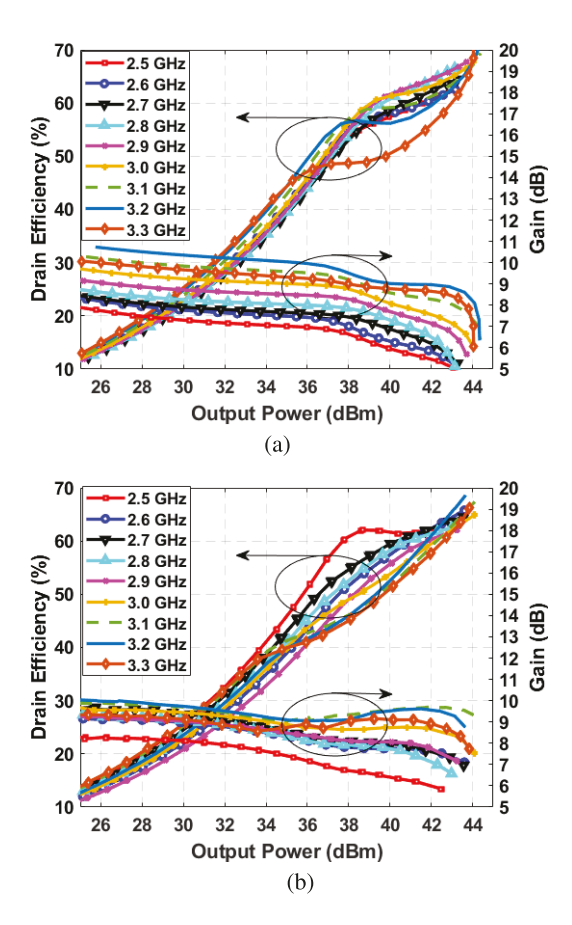


Fig. 15. (a) Simulated drain efficiency and gain (simulations) and (b) measured drain efficiency and gain (measurements).

optimized to track the targeted  $R_{mp}$  trajectory depicted by the blue rectangles. Using the frequency-dependent  $K_{va}(\omega)$ determined in (7),  $\theta_m(\omega)$  and  $\theta_a(\omega)$  dispersion result and shown in Fig. 8(b) from 2.5 to 3.2 GHz. It is worth mentioning that the frequency dependence of  $K_{va}(\omega)$  (indicted by solid red dots and blue rectangles) establishes a quasi-linear phase response versus frequency approaching that of an ideal TL dispersion (indicated by the red dash-dotted and blue dashed lines), which greatly facilitates the combiner design outlined next. The linear parasitic L-C model of this GaN device [43] is incorporated in the design to move the design from the package to the current source reference planes. Alternatively, instead of performing the circuits' design and optimization shown in Fig. 7, the main and auxiliary PA output branches can be modeled as a network of lossy TLs with equivalent characteristic impedance  $Z_0$  and electrical length  $\phi$  given

A Chebyshev post-matching transformer and the drain bias circuits as shown in Fig. 7(b) are co-designed to transform the output  $50-\Omega$  load to  $R_L$  summarized in Table I across the entire frequency band. The simulated frequency-dependent  $R_L$  is indicated by the blue dash trajectory in the *zoomed-in* Smith chart in Fig. 8(c), which are closely tracking the targeted design goals (blue hollow circle). A parallel R-C network  $(2 \text{ pF} // 50 \Omega)$  is used to stabilize the PA. A low-Q broadband input matching circuit is then implemented to transform the device's gate input impedance to approximately 50  $\Omega$  from

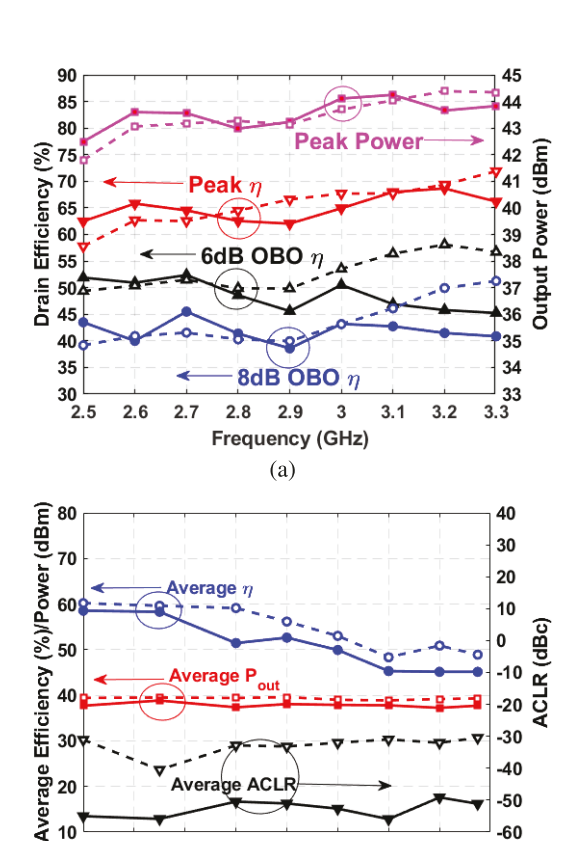


Fig. 16. (a) Measured (solid line) and simulated (dashed line) PA performances using CW signals and (b) measured PA performance using 20-MHz LTE signals with 6.1-dB PAPR before (dashed line) and after DPD (solid line). (a) CW measurements. (b) 20-MHz LTE signal measurements.

Frequency (GHz) (b)

2.8 2.9 3

2.5 2.6 -60

3.2 3.3

2.5 to 3.2 GHz. A 50- $\Omega$  TL as shown in Fig. 9 is used as the PA input phase shifter to match the required theoretical frequency-dependent input phase offset  $\theta_{p4}$  shown in Fig. 10.

It is noted that the theoretical input phase offset (marked with black dots) is different from the final determined phase angles (marked by the dashed lines) due to the nonlinear embedding [45] and linear embedding process introduced by the input matching network. A symmetric Wilkinson power divider is used to split the incident power evenly from 2.5 to 3.2 GHz. The simplified schematic of the proposed wideband  $HD\omega$ -PA is shown in Fig. 11. The final fabricated  $HD\omega$ -PA circuit and the large signal network analyzer (LSNA) PA testbench are shown in Fig. 12(a) and (b), respectively. This PA was built on a Rogers IsoClad 917 substrate with a relative dielectric constant of 2.2 and a thickness of 31 mil. Two Wolfspeed's gallium nitride (GaN) high-electron-mobility transistors (HEMTs) CGH40010F are used for both the main and auxiliary PAs. The gate bias voltage for the main PA is -3.0 V with a dc quiescent current of 55 mA. The gate bias voltage for the auxiliary PA is set to be -5.7 V. The main and auxiliary PAs share the same dc drain bias of 28 V.

# IV. SIMULATION AND MEASUREMENT RESULTS

The simulated and measured small-signal performance of the fabricated PA is shown in Fig. 13 (a) and (b). The simulated

TABLE II MODULATED SIGNAL MEASUREMENTS USING 50-MHz OFDM SIGNAL

	$f_0$	PAPR	Pout,avg.	$\eta_{avg}$ .	$ACLR_{L,H}$	NMSE	EVM
	(GHz)	(dB)	(dBm)	(%)	(dBc)	(dB)	(%)
Before DPD	2.6	10.2	34.6	43.9	-35.4, -31.3	-17.9	5.81
After DPD	2.6	10.2	33.8	40.7	-44.4, -44.7	-37.0	1.35
Before DPD	2.9	10.2	35.3	44.9	-34.4, -35.9	-14.6	5.25
After DPD	2.9	10.2	33.9	39.6	-44.9, -45.0	-36.6	1.47
Before DPD	3.15	10.2	34.8	38.5	-30.8, -37.0	-12.9	6.6
After DPD	3.15	10.2	33.0	33.0	-47.1, -44.4	-34.2	1.25

TABLE III COMPARISON BETWEEN THE RECENT DESIGN OF LOAD-MODULATED PAS

Architecture Frequency		$P_{\rm sat}$	PAPR	ACLR	FBW	$\eta_{\mathbf{avg}}$	Reference
N/A	(GHz)	(dBm)	(dB)	(dBc)	(%)	(%)	N/A
Doherty	4.7-5.3	39.0-39.5	7.4	-52.7	12	38.9-43.6	[19]
Doherty	1.35-1.7	42.0	6.0	-50	23	59.0-62.0	[18]
Doherty	2.80-3.55	43.0-45.0	6.5	-51.4	23.6	49.1-57.2	[22]
Doherty	2.55-3.35	44.3-45.4	8.0	-51.1	27.1	53.4-56.6	[23]
Doherty	1.4-2.5	44-45.9	9.0	-47.4	56.4	57.4-53.5	[27]
LMBA	1.45-2.45	45.6-46.7	6.0	-49.0	51.3	51.2-64.4	[31]
OLMBA	0.65-3.25	45.0-47.0	N/A	N/A	135.0	50.0-70.0	[32]
DEPA	2.55-3.8	48.8-49.8	8.0	-51.3	40.0	47-60	[25]
$HD\omega$ -PA	2.5-3.3	42.5-44.2	6.1	-55.9	27.6	45.1-58.5	This work

load modulation trajectories versus frequency seen by the main and auxiliary PAs are shown in Fig. 14. It is noted that these simulations are based on the fabrication-ready PA EM model. Then the PA was evaluated from 2.5 to 3.3 GHz using continuous-wave (CW) signals. Fig. 15(a) and (b) depicts the simulated and measured drain efficiency and gain versus output power from 2.5 to 3.3 GHz, respectively. Based on Fig. 16(a), the CW-measured 6-dB backoff drain efficiency is from 45% to 52%, the 8-dB backoff drain efficiency is from 40% to 45%, and the measured saturation power is between 42.5 and 44.2 dBm. The measured data and simulated data are comparable.

This PA is also evaluated using modulated signals for different carrier frequencies from 2.5 to 3.3 GHz. According to Fig. 16(b), adjacent channel leakage ratios (ACLRs) less than -50 dBc and average efficiencies from 45% to 59% are observed across the entire frequency band after the digital predistortion (DPD). The generalized cubic spine basis DPD reported in [48] is adopted in this work. It is noted that these experiments were conducted using a 20-MHz LTE signal with 6.1-dB peak-to-average-power ratio (PAPR). Furthermore, a 5G-like 50-MHz orthogonal frequency-division multiplexing (OFDM) signal with 10.1-dB PAPR is applied to test the PA's linearity performance at 2.6, 2.9, and 3.15 GHz. The output spectral density and constellation diagram are shown in Fig. 17(a)–(e). It is worth pointing out that there exists asymmetry on the spectrum regrowth of the output spectrum before DPD, which could be obviated by properly designing

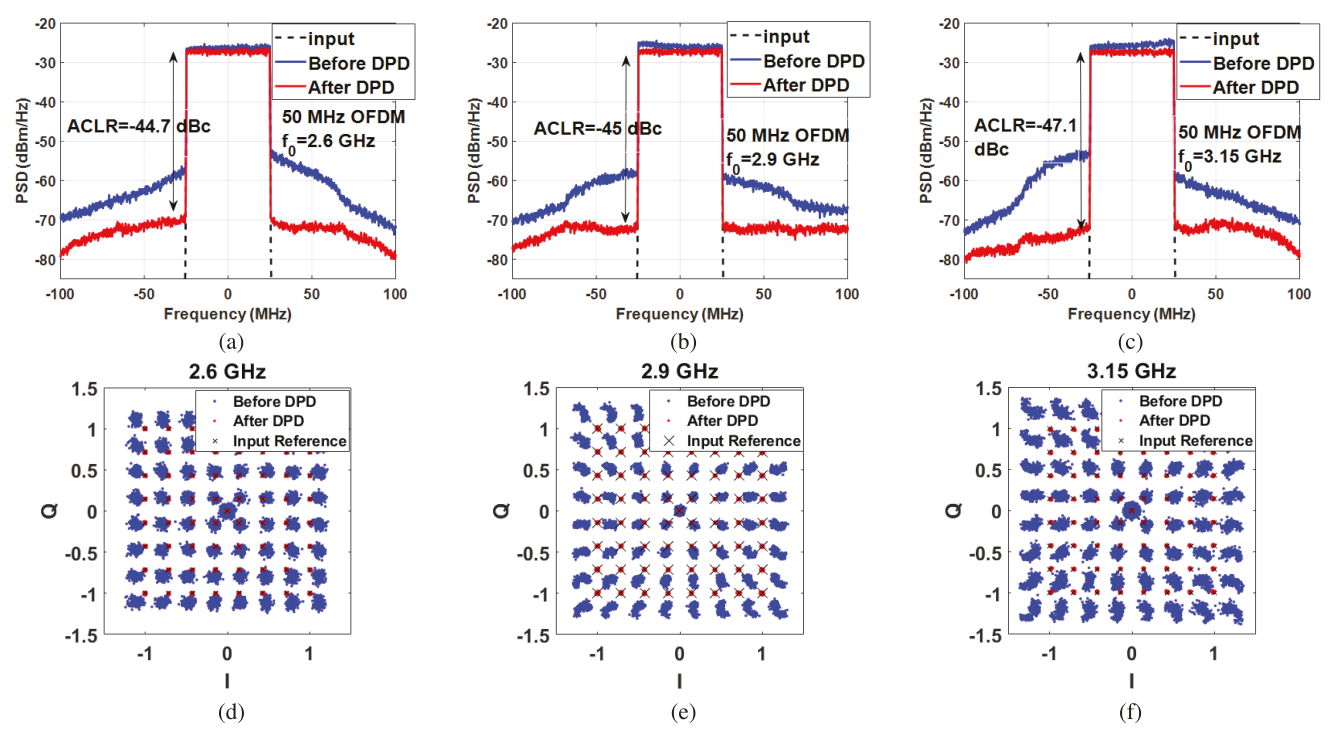


Fig. 17. Output spectral density indicating the ACLR before and after DPD and constellation diagram indicating the EVM before and after DPD. (a) 2.6 GHz. (b) 2.9 GHz. (c) 3.15 GHz. (d) 2.6 GHz. (e) 2.9 GHz. (f) 3.15 GHz.

the baseband impedance and tuning the bias points [49]. The measured performance for this 50-MHz OFDM signal before and after DPD is also summarized in Table II. Table III shows comparison of the performance of the proposed HD $\omega$ -PA with other recent wideband single-input load-modulated PAs found in the literature.

#### V. CONCLUSION

A single-input broadband hybrid Doherty PA design theory with constant output backoff was introduced. In this single-input hybrid Dohert PA theory, the broadband load modulation is realized by monotonously sliding the value of the auxiliary PA peak-to-backoff voltage ratio  $K_{va}$  versus frequency, to track the Doherty to HDmax PA-mode continuum. The analytic equations are reported in this article to determine the frequency dependence of  $K_{va}$  required for broadband phase sliding-mode operation for both the constant OBO and constant saturated power cases. After the theoretical analysis and comparison, the constant OBO case selected in this work, out of the eight possible input phase offset angles, it was demonstrated that only one solution leads to both: 1) a compact circuit design for the output combiner and input phase shifter and 2) yielded a relatively constant saturated (peak) power versus frequency for the single-input PA. A wideband PA combiner circuit was then designed to maintain the correct load modulation behavior across the entire targeted frequency band. The input phase shifter was designed to provide the correct input phase offset at each frequency. A demonstrator PA circuit was fabricated and evaluated from 2.5 to 3.3 GHz using both CW and 4G and 5G modulated signals to validate the proposed theory and design methodology.

# REFERENCES

- [1] W. H. Doherty, "A new high efficiency power amplifier for modulated waves," *Proc. IRE*, vol. 24, no. 9, pp. 1163–1182, Sep. 1936.
- [2] F. H. Raab, "Efficiency of Doherty RF power-amplifier systems," *IEEE Trans. Broadcast.*, vol. BC-33, no. 3, pp. 77–83, Sep. 1987.
- [3] M. Iwamoto, A. Williams, P.-F. Chen, A. G. Metzger, L. E. Larson, and P. M. Asbeck, "An extended Doherty amplifier with high efficiency over a wide power range," *IEEE Trans. Microw. Theory Techn.*, vol. 49, no. 12, pp. 2472–2479, Dec. 2001.
- [4] B. Kim, J. Kim, I. Kim, and J. Cha, "The Doherty power amplifier," *IEEE Microw. Mag.*, vol. 7, no. 5, pp. 42–50, Oct. 2006.
- [5] A. Grebennikov and S. Bulja, "High-efficiency Doherty power amplifiers: Historical aspect and modern trends," *Proc. IEEE*, vol. 100, no. 12, pp. 3190–3219, Dec. 2012.
- [6] M. Özen, K. Andersson, and C. Fager, "Symmetrical Doherty power amplifier with extended efficiency range," *IEEE Trans. Microw. Theory Techn.*, vol. 64, no. 4, pp. 1273–1284, Apr. 2016.
- [7] J. M. Rubio, J. Fang, V. Camarchia, R. Quaglia, M. Pirola, and G. Ghione, "3–3.6-GHz wideband GaN Doherty power amplifier exploiting output compensation stages," *IEEE Trans. Microw. Theory Techn.*, vol. 60, no. 8, pp. 2543–2548, Aug. 2012.
- [8] K. Bathich, A. Z. Markos, and G. Boeck, "Frequency response analysis and bandwidth extension of the Doherty amplifier," *IEEE Trans. Microw. Theory Techn.*, vol. 59, no. 4, pp. 934–944, Apr. 2011.
- [9] D. Y.-T. Wu and S. Boumaiza, "A modified Doherty configuration for broadband amplification using symmetrical devices," *IEEE Trans. Microw. Theory Techn.*, vol. 60, no. 10, pp. 3201–3213, Oct. 2012.
- [10] R. Giofre, L. Piazzon, P. Colantonio, and F. Giannini, "An ultra-broadband GaN Doherty amplifier with 83% of fractional bandwidth," *IEEE Microw. Wireless Compon. Lett.*, vol. 24, no. 11, pp. 775–777, Nov. 2014.
- [11] R. Giofrè, L. Piazzon, P. Colantonio, and F. Giannini, "A closed-form design technique for ultra-wideband Doherty power amplifiers," *IEEE Trans. Microw. Theory Techn.*, vol. 62, no. 12, pp. 3414–3424, Dec. 2014.
- [12] J. Pang, S. He, C. Huang, Z. Dai, J. Peng, and F. You, "A post-matching Doherty power amplifier employing low-order impedance inverters for broadband applications," *IEEE Trans. Microw. Theory Techn.*, vol. 63, no. 12, pp. 4061–4071, Dec. 2015.
- [13] J. Xia, M. Yang, Y. Guo, and A. Zhu, "A broadband high-efficiency Doherty power amplifier with integrated compensating reactance," *IEEE Trans. Microw. Theory Techn.*, vol. 64, no. 7, pp. 2014–2024, Jul. 2016.

- [14] X. Chen, W. Chen, F. M. Ghannouchi, Z. Feng, and Y. Liu, "A broad-band Doherty power amplifier based on continuous-mode technology," *IEEE Trans. Microw. Theory Techn.*, vol. 64, no. 12, pp. 4505–4517, Dec. 2016.
- [15] X. Y. Zhou, S. Y. Zheng, W. S. Chan, S. Chen, and D. Ho, "Broadband efficiency-enhanced mutually coupled harmonic postmatching Doherty power amplifier," *IEEE Trans. Circuits Syst. I, Reg. Papers*, vol. 64, no. 7, pp. 1758–1771, Jul. 2017.
- [16] W. Shi et al., "Broadband continuous-mode Doherty power amplifiers with noninfinity peaking impedance," *IEEE Trans. Microw. Theory Techn.*, vol. 66, no. 2, pp. 1034–1046, Feb. 2018.
- [17] S. Ghosh and K. Rawat, "Hybrid analog/digital continuous class B/J mode for broadband Doherty power amplifiers," *IEEE Access*, vol. 7, pp. 74986–74995, 2019.
- [18] X.-H. Fang, H.-Y. Liu, K.-K.-M. Cheng, and S. Boumaiza, "Two-way Doherty power amplifier efficiency enhancement by incorporating Transistors' nonlinear phase distortion," *IEEE Microw. Wireless Compon. Lett.*, vol. 28, no. 2, pp. 168–170, Feb. 2018.
- [19] X. Fang, A. Chung, and S. Boumaiza, "Linearity-enhanced Doherty power amplifier using output combining network with predefined AM– PM characteristics," *IEEE Trans. Microw. Theory Techn.*, vol. 67, no. 1, pp. 195–204, Jan. 2019.
- [20] M. Ruhul Hasin and J. Kitchen, "Exploiting phase for extended efficiency range in symmetrical Doherty power amplifiers," *IEEE Trans. Microw. Theory Techn.*, vol. 67, no. 8, pp. 3455–3463, Aug. 2019.
- [21] S. Hu, F. Wang, and H. Wang, "A 28-/37-/39-GHz linear Doherty power amplifier in silicon for 5G applications," *IEEE J. Solid-State Circuits*, vol. 54, no. 6, pp. 1586–1599, Jun. 2019.
- [22] M. Li, J. Pang, Y. Li, and A. Zhu, "Bandwidth enhancement of Doherty power amplifier using modified load modulation network," *IEEE Trans. Circuits Syst. I, Reg. Papers*, vol. 67, no. 6, pp. 1824–1834, Jun. 2020.
- [23] J. Pang, Y. Li, C. Chu, J. Peng, X. Y. Zhou, and A. Zhu, "Extend high efficiency range of Doherty power amplifier by modifying characteristic impedance of transmission lines in load modulation network," in *IEEE MTT-S Int. Microw. Symp. Dig.*, Aug. 2020, pp. 707–710.
- [24] X. Zhou, W. S. Chan, T. Sharma, J. Xia, S. Chen, and W. Feng, "A Doherty power amplifier with extended high-efficiency range using three-port harmonic injection network," *IEEE Trans. Circuits Syst. I, Reg. Papers*, vol. 69, no. 7, pp. 2756–2766, Jul. 2022.
- [25] P. Saad, R. Hou, R. Hellberg, and B. Berglund, "The continuum of load modulation ratio from Doherty to traveling-wave amplifiers," *IEEE Trans. Microw. Theory Techn.*, vol. 67, no. 12, pp. 5101–5113, Dec. 2019.
- [26] P. Saad, R. Hou, R. Hellberg, and B. Berglund, "A 1.8–3.8-GHz power amplifier with 40% efficiency at 8-dB power back-off," *IEEE Trans. Microw. Theory Techn.*, vol. 66, no. 11, pp. 4870–4882, Nov. 2018.
- [27] Y. Xu, J. Pang, X. Wang, and A. Zhu, "Enhancing bandwidth and back-off range of Doherty power amplifier with modified load modulation network," *IEEE Trans. Microw. Theory Techn.*, vol. 69, no. 4, pp. 2291–2303, Apr. 2021.
- [28] H. Lyu, Y. Cao, and K. Chen, "Linearity-enhanced and highly efficient Doherty power amplifier: 16th high efficiency power amplifier student design competition," *IEEE Microw. Mag.*, vol. 22, no. 10, pp. 62–69, Oct. 2021.
- [29] P. E. de Falco et al., "Load modulation of harmonically tuned amplifiers and application to outphasing systems," *IEEE Trans. Microw. Theory Techn.*, vol. 65, no. 10, pp. 3596–3612, Oct. 2017.
- [30] P. H. Pednekar, W. Hallberg, C. Fager, and T. W. Barton, "Analysis and design of a Doherty-like RF-input load modulated balanced amplifier," *IEEE Trans. Microw. Theory Techn.*, vol. 66, no. 12, pp. 5322–5335, Dec. 2018.
- [31] J. Pang, C. Chu, Y. Li, and A. Zhu, "Broadband RF-input continuous-mode load-modulated balanced power amplifier with input phase adjustment," *IEEE Trans. Microw. Theory Techn.*, vol. 68, no. 10, pp. 4466–4478, Oct. 2020.
- [32] D. J. Collins, R. Quaglia, J. R. Powell, and S. C. Cripps, "The orthogonal LMBA: A novel RFPA architecture with broadband reconfigurability," *IEEE Microw. Wireless Compon. Lett.*, vol. 30, no. 9, pp. 888–891, Sep. 2020.
- [33] Y. Cao, H. Lyu, and K. Chen, "Asymmetrical load modulated balanced amplifier with continuum of modulation ratio and dual-octave bandwidth," *IEEE Trans. Microw. Theory Techn.*, vol. 69, no. 1, pp. 682–696, Jan. 2021.
- [34] C. Chu et al., "Waveform engineered sequential load modulated balanced amplifier with continuous class-F-1 and class-J operation," *IEEE Trans. Microw. Theory Techn.*, vol. 70, no. 2, pp. 1269–1283, Feb. 2022.

- [35] R. Darraji, F. M. Ghannouchi, and O. Hammi, "A dual-input digitally driven Doherty amplifier architecture for performance enhancement of Doherty transmitters," *IEEE Trans. Microw. Theory Techn.*, vol. 59, no. 5, pp. 1284–1293, May 2011.
- [36] C. M. Andersson, D. Gustafsson, J. Chani Cahuana, R. Hellberg, and C. Fager, "A 1–3-GHz digitally controlled dual-RF input power-amplifier design based on a Doherty-outphasing continuum analysis," *IEEE Trans. Microw. Theory Techn.*, vol. 61, no. 10, pp. 3743–3752, Oct. 2013.
- [37] Y. Komatsuzaki et al., "A novel 1.4–4.8 GHz ultra-wideband, over 45% high efficiency digitally assisted frequency-periodic load modulated amplifier," in *IEEE MTT-S Int. Microw. Symp. Dig.*, Jun. 2019, pp. 706–709.
- [38] C. Liang, P. Roblin, Y. Hahn, Z. Popovic, and H.-C. Chang, "Novel outphasing power amplifiers designed with an analytic generalized Doherty-Chireix continuum theory," *IEEE Trans. Circuits Syst. I, Reg. Papers*, vol. 66, no. 8, pp. 2935–2948, Aug. 2019.
- [39] C. Liang, T. Niubo-Aleman, Y. Hahn, P. Roblin, and J. A. Reynoso-Hernandez, "Optimal two-way hybrid Doherty-outphasing power amplifier," in *Proc. IEEE Topical Conf. RF/Microw. Power Modeling Radio* Wireless Appl. (PAWR), Jan. 2020, pp. 26–29.
- [40] C. Liang, J. I. Martinez-Lopez, P. Roblin, Y. Hahn, D. Mikrut, and V. Chen, "Wideband two-way hybrid Doherty outphasing power amplifier," *IEEE Trans. Microw. Theory Techn.*, vol. 69, no. 2, pp. 1415–1428, Feb. 2021.
- [41] C. Liang and P. Roblin, "The analytic Doherty-outphasing power amplifiers continuum theory: (Invited paper)," in *Proc. IEEE 22nd Annu. Wireless Microw. Technol. Conf. (WAMICON)*, Apr. 2022, pp. 1–4.
- [42] J. Bachi et al., "A novel approach for Doherty PA design using a compact L-C combiner," *IEEE Trans. Circuits Syst. II, Exp. Briefs*, vol. 69, no. 10, pp. 4023–4027, Oct. 2022.
- [43] P. J. Tasker and J. Benedikt, "Waveform inspired models and the harmonic balance emulator," *IEEE Microw. Mag.*, vol. 12, no. 2, pp. 38–54, Apr. 2011.
- [44] Y. Wu, M. Qu, and Y. Liu, "A generalized lossy transmission-line model for tunable graphene-based transmission lines with attenuation phenomenon," Sci. Rep., vol. 6, no. 1, Oct. 2016, Art. no. 31760.
- [45] H. Jang, P. Roblin, and Z. Xie, "Model-based nonlinear embedding for power-amplifier design," *IEEE Trans. Microw. Theory Techn.*, vol. 62, no. 9, pp. 1986–2002, Sep. 2014.
- [46] C. Liang, T. Niubo-Aleman, Y. Hahn, P. Roblin, and J. A. Reynoso-Hernandez, "Optimal two-way hybrid Dohertyoutphasing power amplifier," in *Proc. IEEE Topical Conf. RF/Microw. Power Modeling Radio Wireless Appl. (PAWR)*, Jan. 2020, pp. 26–29.
- [47] C. Liang, P. Roblin, and Y. Hahn, "Accelerated design methodology for dual-input Doherty power amplifiers," *IEEE Trans. Microw. Theory Techn.*, vol. 67, no. 10, pp. 3983–3995, Oct. 2019.
- [48] H. C. Chang, Y. Hahn, P. Roblin, and T. W. Barton, "New mixed-mode design methodology for high-efficiency outphasing chireix amplifiers," *IEEE Trans. Circuits Syst. I, Reg. Papers*, vol. 66, no. 4, pp. 1594–1607, Apr. 2019.
- [49] N. B. D. Carvalho and J. C. Pedro, "A comprehensive explanation of distortion sideband asymmetries," *IEEE Trans. Microw. Theory Techn.*, vol. 50, no. 9, pp. 2090–2101, Sep. 2002.



Chenyu Liang (Member, IEEE) received the B.S. degree in electrical and computer engineering from New Mexico State University, Las Cruces, NM, USA, in 2013, the B.Eng. degree in electrical engineering from the University of Electronic Science and Technology of China, Chengdu, China, in 2013, and the M.S. and Ph.D. degrees in electrical and computer engineering from The Ohio State University, Columbus, OH, USA, in 2016 and 2020, respectively.

Since 2020, he has been a Senior Design Engineer

with Qorvo US Inc., San Jose, CA, USA, where he is currently involved in RF/mmWave IC power amplifiers design. His main research interests include sub-6-GHz high-efficiency and linearity GaN Doherty power amplifiers for massive MIMO applications and GaAs RF/millimeter-wave IC power amplifier for 5G handset applications.

Dr. Liang serves as an Affiliate Member for the Technical Committee for IEEE MTT-S 12 Microwave High-Power Techniques Committee. He was a recipient of the 2019 Fall Outstanding Teaching Assistant Award of the Department of Electrical and Computer Engineering, The Ohio State University.



Patrick Roblin (Senior Member, IEEE) received the maitrise de physics degree from Louis Pasteur University, Strasbourg, France, in 1980, and the M.S. and D.Sc. degrees in electrical engineering from Washington University, St. Louis, MO, USA, in 1982 and 1984, respectively.

In 1984, he joined the Department of Electrical Engineering, The Ohio State University (OSU), Columbus, OH, USA, as an Assistant Professor, where he is currently a Professor. He is the Lead Author of the *High-Speed Heterostructure and* 

Devices (Cambridge University Press, 2002) and Nonlinear RF Circuits and Nonlinear Vector Network Analyzers (Cambridge University Press, 2011). He is currently the Founder of the Non-Linear RF Research Laboratory, OSU. His current research interests include measurement, modeling, design, and linearization of nonlinear RF devices and circuits, such as oscillators, mixers, and power amplifiers.

Dr. Roblin served as a Distinguished Microwave Lecturer in 2016, 2017, and 2018.



Yunsik Hahn (Graduate Student Member, IEEE) was born in Seoul, Republic of Korea. He received the B.Eng. degree in electronic engineering from Dong-A University, Busan, Republic of Korea, in 2012. He is currently pursuing the Ph.D. degree in electrical and computer engineering at The Ohio State University, Columbus, OH, USA.

His main research interests include linearization of high-efficiency nonlinear power amplifiers with DPD techniques.



Jose I. Martinez-Lopez (Member, IEEE) was born in Mexico City, Mexico. He received the B.S., M.Eng., and Ph.D. degrees in electrical engineering from the National Autonomous University of Mexico (UNAM), Mexico City, Mexico, in 1994, 1998, and 2005, respectively.

In 2006, he was with the Schlumberger Technology Center, Sugar Land, TX, USA, developing antennas for deep induction array tools for the oil industry. In 2009, he was a Visiting Scholar for one year with the ElectroScience Laboratory, The

Ohio State University (OSU), Columbus, OH, USA. From 2019 to 2021, he was a Visiting Professor with the Nonlinear RF Laboratory, Department of Electrical and Computer Engineering, OSU. He is currently a Professor of electrical engineering with UNAM. His current research interests include antenna arrays, frequency selective surfaces, and microwave and millimeterwave circuits.



Hsiu-Chen Chang (Graduate Student Member, IEEE) received the M.Sc. degree in electro-optical engineering from the National Taiwan University of Science and Technology (NTUST), Taipei, Taiwan, in 2009, and the Ph.D. degree in electrical and computer engineering from The Ohio State University, Columbus, OH, USA, in 2020.

He was a Research and Development Engineer with WIN Semiconductors, Taoyuan, Taiwan, where he was developing HBT MMIC power amplifiers. In 2021, he joined Skyworks Solutions, Irvine, CA,

USA, as an Electrical Staff Engineer. His current research interests include broadband high-efficiency outphasing and Doherty power amplifiers' design, linearization, and measurements of nonlinear RF/microwave devices and circuits.



Vanessa Chen (Member, IEEE) received the Ph.D. degree in electrical and computer engineering from Carnegie Mellon University, Pittsburgh, PA, USA, in 2013.

She was with Qualcomm, San Diego, CA, USA, working on energy-efficient data-acquisition systems for mobile devices. She was an Assistant Professor with The Ohio State University, Columbus, OH, USA. From 2010 to 2013, at Carnegie Mellon, she focused her research on self-healing systems and high-speed ADCs, and held a research internship

position with the IBM T. J. Watson Research Center, Yorktown Heights, NY, USA, in 2012. She is currently an Assistant Professor of electrical and computer engineering with Carnegie Mellon University, Pittsburgh, PA, USA. Her research interests focus on data conversion interfaces for machine learning, RF/analog hardware security, ubiquitous sensing, and communication systems.

Dr. Chen is a Technical Program Committee Member of the IEEE Custom Integrated Circuits Conference (CICC) and the IEEE Asian Solid-State Circuits Conference (A-SSCC). She was a recipient of the NSF CAREER Award in 2019, the Analog Devices Outstanding Student Designer Award in 2013, and the IBM Ph.D. Fellowship in 2012. She is also an Associate Editor of the IEEE OPEN JOURNAL OF CIRCUITS AND SYSTEMS.